Single-molecule imaging of transcription factor binding to DNA in live mammalian cells

J Christof M Gebhardt[1,5], David M Suter[1,5], Rahul Roy[1,4], Ziqing W Zhao[1,2], Alec R Chapman[1,2], Srinjan Basu[1,3,4], Tom Maniatis[3] & X Sunney Xie[1]

Imaging single fluorescent proteins in living mammalian cells is challenged by out-of-focus fluorescence excitation. To reduce out-of-focus fluorescence we developed reflected light-sheet microscopy (RLSM), a fluorescence microscopy method allowing selective plane illumination throughout the nuclei of living mammalian cells. A thin light sheet parallel to the imaging plane and close to the sample surface is generated by reflecting an elliptical laser beam incident from the top by 90° with a small mirror. The thin light sheet allows for an increased signal-to-background ratio superior to that in previous illumination schemes and enables imaging of single fluorescent proteins with up to 100-Hz time resolution. We demonstrated the single-molecule sensitivity of RLSM by measuring the DNA-bound fraction of glucocorticoid receptor (GR) and determining the residence times on DNA of various oligomerization states and mutants of GR and estrogen receptor-α (ER), which permitted us to resolve different modes of DNA binding of GR. We demonstrated two-color single-molecule imaging by observing the spatiotemporal colocalization of two different protein pairs. Our single-molecule measurements and statistical analysis revealed dynamic properties of transcription factors.

Tracking single molecules in living cells provides a direct way to probe the kinetics of their interactions with other cellular components and is particularly useful for characterizing unsynchronized dynamic events[1]. This applies well to the study of mammalian transcription factors, which have recently been shown to interact with DNA in a dynamic manner[2], suggesting the need for new models of transcription initiation[3]. The imaging of single fluorescent fusion proteins has provided valuable insight into the dynamic properties of transcription and translation in living bacterial cells[4,5], but it remains challenging to observe single biomolecules in the nuclei of much larger living mammalian cells.

Whereas low concentrations of single intracellular fluorescent molecules can be visualized using wide-field illumination[6,7], distinguishing higher concentrations of single molecules requires a smaller excitation volume. Total internal reflection fluorescence microscopy illuminates a thin section close to the sample surface and enables visualization of single fluorescent molecules in the cell membrane[8]. However, this type of microscopy cannot be used to achieve selective excitation in the cell nucleus. An increase in signal-to-background ratio (SBR) has been achieved with highly inclined and laminated optical sheet (HILO) microscopy[9]; unfortunately, reduction of the light-sheet thickness in HILO microscopy is proportional to a decrease in the illuminated area in the focal plane. Moreover, the inclined nature of the illuminating laser beam still leads to out-of-focus fluorescence excitation.

The selective plane illumination scheme allows for an additional decrease of the illuminated volume and restricts sample excitation to the focal plane[10]. Microscopists have used this principle to image living embryos with minimal photodamage by illuminating the sample from the side with an objective placed orthogonal to the detection objective[10]. Subsequently, diffusion of single quantum dots has been imaged in developing zebrafish[11], diffusion of dye-labeled single molecules has been observed in real time in large salivary gland nuclei[12], and super-resolution microscopy has been performed with photoactivatable fluorescent proteins in cellular spheroids[13]. To image small mammalian cells with selective plane illumination, two objectives with low numerical aperture (NA) have been used to section the cell at 45° with respect to the sample surface[14,15]. With a similar arrangement of objectives, the light sheet recently has been replaced by an illumination scheme based on Bessel beams[16]. However, single-molecule detection has not yet been reported with this configuration of objectives, probably because only objectives with low NA (<0.8), which are not optimal for single-molecule imaging, can be used.

Here we report an illumination scheme that combines selective plane illumination with a vertical arrangement of illumination and detection objectives. In this geometry, a disposable mirror reflects the light sheet into a horizontal plane close to the sample surface, thus allowing horizontal sectioning of the cells and the use of a high-NA objective for detection of fluorescence. With our

[1]Department of Chemistry and Chemical Biology, Harvard University, Cambridge, Massachusetts, USA. [2]Graduate Program in Biophysics, Harvard University, Cambridge, Massachusetts, USA. [3]Department of Biochemistry and Molecular Biophysics, Columbia University Medical Center, New York, New York, USA. [4]Present addresses: Department of Chemical Engineering, Indian Institute of Science, Bangalore, India (R.R.), and Department of Biochemistry, University of Cambridge, Cambridge, UK (S.B.). [5]These authors contributed equally to this work. Correspondence should be addressed to X.S.X. (xie@chemistry.harvard.edu).

RECEIVED 24 SEPTEMBER 2012; ACCEPTED 26 FEBRUARY 2013; PUBLISHED ONLINE 24 MARCH 2013; DOI:10.1038/NMETH.2411

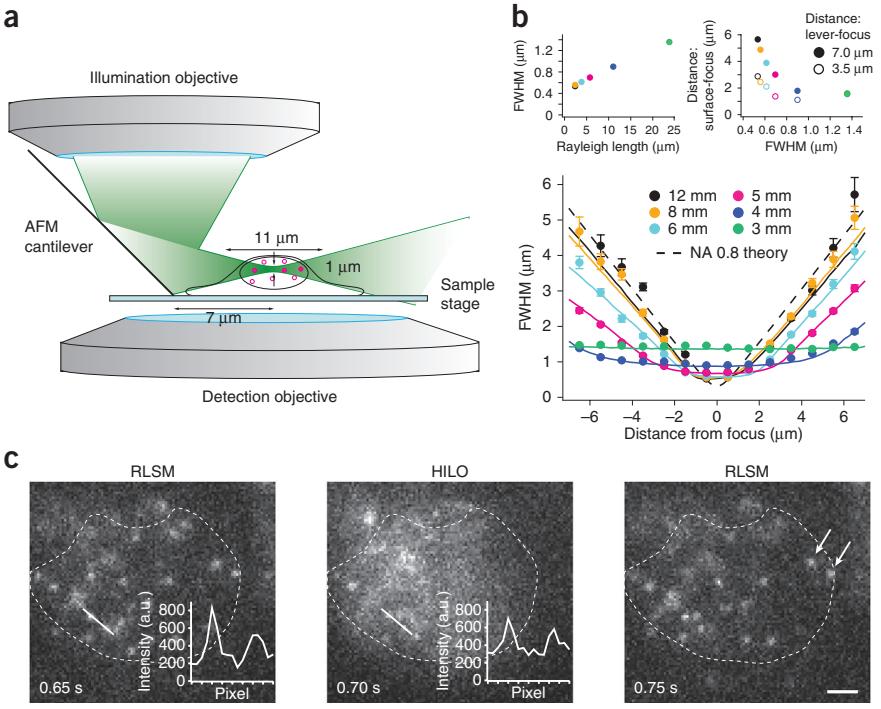

Figure 1 | Visualization of single fluorescently labeled DNA binding proteins by RLSM. (**a**) Scheme of the reflected light-sheet principle (not drawn to scale). A laser beam is focused by an objective to form a vertical light sheet that is reflected by 90° off an AFM cantilever next to a cell in a Petri dish. Fluorescence is detected by a second high-NA objective. Three-dimensional optical sectioning is achieved through vertical displacement of the sample. (**b**) Bottom, FWHM of the light sheet before (solid lines) and after (symbols) reflection as function of the distance from the focus, shown at different aperture diameters. The dashed line indicates the beam profile expected for an objective with an NA of 0.8. Error bars, s.d. (Online Methods). Top left, FWHM of the light sheet at the focus as a function of the Rayleigh length for different aperture diameters. Top right, minimal distance between the surface and focus as a function of the FWHM for different aperture diameters and distances between the cantilever edge and focus. (**c**) Alternate RLSM and HILO microscopy images of an MCF-7 cell expressing mEos2–histone H4 with 50-ms time resolution ~6 µm above the coverslip. Insets (left and middle) indicate the fluorescence intensity along the white line. Arrows (right) indicate mEos2 molecules detected with RLSM but overlooked by HILO microscopy. The dashed line outlines the nuclear envelope. a.u., arbitrary units. Scale bar, 2 µm.

setup, we imaged single fluorescent proteins in live mammalian cells with high SBR and millisecond time resolution.

We demonstrated the potential of our microscopy method, RLSM, by directly monitoring the binding properties of fluorescently labeled GR and ER to DNA. GR is a transcription factor that localizes mostly to the cytoplasm in the absence of hormone but forms homodimers and translocates into the nucleus upon binding to glucocorticoids[17]. Previous studies have shown that dimeric GR binds directly to DNA at regulatory sequences, whereas the monomer can be indirectly recruited to DNA by other DNA-bound protein complexes[18]. The mode of DNA interaction defines whether the target gene is activated or repressed. We found that the residence times of monomeric GR and indirectly bound GR were only 10% and 50%, respectively, of the residence time of the dimeric transcription factor. We obtained a similar result for ER. Finally, we demonstrated the capability of RLSM for two-color single-molecule imaging. This allowed us to directly observe spatiotemporal colocalization of GR and its coactivator GRIP1 and of the heterodimeric transcription factor pair BMAL1 and CLOCK. The imaging technique described here will be generally applicable to single-molecule studies in living mammalian cells.

RESULTS

Setup of the reflected light-sheet microscope

In selective-plane-illumination microscopes, two orthogonal objectives are used[19]. Because of spatial constraints imposed by the objectives, the light sheet can be positioned only at distances >10 µm above the sample surface, and the full width at half maximum (FWHM) of the light sheet is >2 µm (ref. 12). Selective illumination of typical mammalian cell nuclei is not possible with this geometry. We overcame this problem by replacing the condenser of an inverted microscope with a vertically mounted high-NA water-immersion objective (**Fig. 1a**, Online Methods, **Supplementary Fig. 1** and **Supplementary Video 1**). This objective focuses an elliptical laser beam incident from the top to form a diffraction-limited sheet of light with an FWHM >0.5 µm (**Fig. 1b**). A small mirror reflects the light sheet by 90° and projects it horizontally into the nucleus of the cell, thus allowing submicrometer optical sectioning. Vertical scanning is achieved by mounting the sample on an *x-y-z* piezo stage. Wide-field imaging of fluorescent light by a second high-NA objective enables high sensitivity and temporal resolution. Owing to the upright geometry of the illumination and detection objectives, standard glass-bottom dishes can be used to both grow and image mammalian cells, thereby simplifying experimental procedures.

We used a disposable tipless atomic force microscopy (AFM) cantilever coated with an aluminum layer to reflect the laser beam (Online Methods). We used the signal from small fluorescent beads to compare the dimensions of the laser beam in the vicinity of the focus before and after reflection (**Fig. 1b**; see Online Methods and **Supplementary Fig. 2**). As expected, the reflection did not alter the shape of the laser beam. Different AFM cantilevers exhibited similar performance (data not shown). By changing the dimensions of the incident beam with a spherical aperture in front of the focusing objective, users can control the Rayleigh length over which the light sheet maintains a relatively constant thickness (**Fig. 1b**). Because of the shape of the light sheet, a small gap between the surface and light sheet cannot be illuminated (**Fig. 1b**). We performed measurements at an aperture size of 4 mm, corresponding to a FWHM of the light sheet of ~1 µm and a Rayleigh length of ~11 µm.

We compared the single-molecule detection capability of RLSM with that of HILO illumination. For the HILO measurements, we chose a small illumination area of ~10 μm to keep the light-sheet thickness small (~5 μm)[9]. We expressed histone H4 fused to the photoactivatable fluorescent protein mEos2 in MCF-7 cells (Online Methods). We activated a subset of mEos2 molecules with a 405-nm laser in the HILO illumination mode and subsequently imaged the fluorescence excited with a 560-nm laser by alternating every 50 ms between RLSM and HILO modes. At low mEos2 activation and close to the coverslip, RLSM resulted in an SBR 1.5 ± 0.1-fold (± s.e.m., n = 3,504 molecules, 8 cells) higher than that with HILO microscopy (**Fig. 1c** and Online Methods). At high activation densities, the SBR obtained with RLSM microscopy was 5.3 ± 0.4-fold higher (± s.e.m., n = 267 molecules, 3 cells; **Supplementary Fig. 3**). Moreover, RLSM allowed detection of single molecules throughout the cross-section of the nucleus, whereas the illuminated area was restricted to a central part of the cross-section for HILO microscopy (**Fig. 1c**). We confirmed the superior SBR and field of view of RLSM throughout the nucleus in different z sections (**Supplementary Fig. 4**).

DNA-bound fractions of transcription factors

We tested different fluorescent fusion partners for single-molecule observations in living cells. In principle, the protein fusion tags SNAP and Halo, which can be covalently labeled with organic dyes, are an attractive labeling strategy because of the brightness and photostability of organic dyes[20–22]. Unfortunately, we found that both SNAP and Halo proteins exhibited stable binding events in the nucleus (**Supplementary Videos 2** and **3**). This intrinsic binding would bias the kinetic analysis of DNA interactions of protein fusion partners; we therefore chose the bright fluorescent proteins mEos2 and YPet as labels for transcription factors, as neither of them exhibited nuclear binding (**Supplementary Videos 4** and **5**). In addition, we used the fluorescent proteins EGFP and TagRFP-T as candidates for two-color applications because of their spectral separation.

To study the diffusion of GR in the nucleus, we expressed an mEos2-GR fusion protein in MCF-7 cells with and without treatment with 100 nM of the hormone analog dexamethasone. We photoactivated only a small subset of mEos2 molecules in the focal plane to limit the number of simultaneously observable molecules and thereby avoid overlap of their trajectories[23], and we imaged single fluorescent proteins with 10-ms time resolution (**Supplementary Video 6**).

We analyzed the diffusion trajectories of nuclear GR (**Fig. 2a**). Each time a molecule was photoactivated in the field of view, we determined the cumulative distribution function of its squared displacement during a fixed time interval of 10 ms (Online Methods)[24]. We observed a higher fraction of small displacements for induced GR in the presence of 100 nM dexamethasone than for uninduced GR (**Fig. 2b**). The cumulative distribution functions deviated from an exponential form expected for Brownian motion (equation (1) in Online Methods). This suggests that a GR molecule undergoes transitions between different states (unbound and bound to DNA) with different diffusion constants. Both distributions can be well fit with three exponential components, corresponding to three effective diffusion constants D_1–D_3 and amplitudes A_1–A_3 (equation (2) in Online Methods). We measured $D_1 = 0.13 \pm 0.03$ μm^2 s^{-1} ($A_1 = 12\% \pm 2\%$), $D_2 = 1.6 \pm 0.3$ μm^2 s^{-1} ($A_2 = 52\% \pm 5\%$) and $D_3 = 8.9 \pm 3.0$ μm^2 s^{-1} ($A_3 = 36\% \pm 6\%$) for

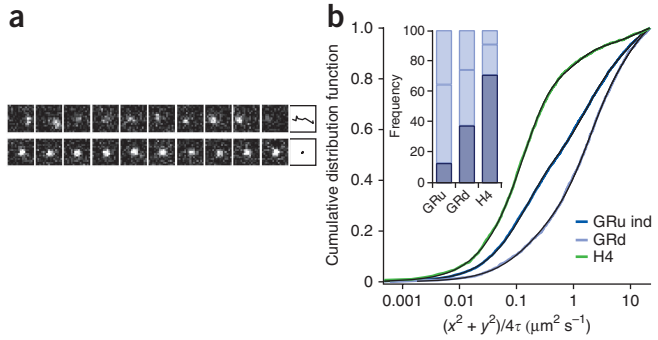

Figure 2 | Characterization of *in vivo* transcription factor diffusion. (**a**) Examples of single-molecule tracking of a fast-diffusing mEos2-GR molecule (top) and of a DNA-bound molecule (bottom) in presence of 100 nM dexamethasone at 10-ms time resolution. Far right, identified traces. (**b**) Cumulative distribution functions of squared displacements of mEos2–histone H4 (H4) and mEos2-GR with (GRd) or without (GRu) 100 nM dexamethasone treatment (n = 3,336, 7 cells (GRd); n = 1,644, 4 cells (GRu); n = 2,020, 8 cells (H4)). Black lines indicate fits with three effective diffusion components to the distributions (equation (2) in Online Methods). Inset, fractions of molecules exhibiting slow effective diffusion corresponding to the DNA-bound fraction (dark blue) and of molecules exhibiting the two fast effective diffusion components (light blue).

uninduced GR and similar values of $D_1 = 0.13 \pm 0.01$ μm^2 s^{-1} (A_1=37% ± 2%), $D_2 = 1.4 \pm 0.2$ μm^2 s^{-1} (A_2 = 37% ± 3%) and $D_3 = 9.2 \pm 2.3$ μm^2 s^{-1} (A_3 = 26% ± 4%) for induced GR (± s.d.; Online Methods). In a recent study on dye-labeled STAT1, effective diffusion constants in the nucleus had been observed that are very similar to those reported here[25].

To assign the slow component, we repeated the measurement for a fusion of mEos2 to histone H4, which is stably incorporated into chromatin (**Fig. 2b**). We again found three diffusion components, with the slowest component $D_1 = 0.13 \pm 0.01$ μm^2 s^{-1} having the highest amplitude of 71% ± 4% (± s.d.; Online Methods). The movement of chromatin in mammalian cells has been observed with diffusion constants ranging from 10^{-4} μm^2 s^{-1} to 10^{-3} μm^2 s^{-1} (ref. 26), slower than D_1. We calculated a localization error of Δx = 49 nm at the photon count of 27.5 within 10 ms for histone H4 (ref. 27). Such average displacement corresponds to an apparent diffusion constant of 0.06 μm^2 s^{-1}, close to D_1. Thus, we conclude that the apparent slow component arises from the localization uncertainty of DNA-bound fluorescent molecules at low signal levels. The larger effective diffusion constants presumably arise from transient nonspecific interactions with DNA and spatially restricted diffusion in the nucleus[28].

We used the amplitude of the slowest diffusion component as an estimate for the DNA-bound fraction of the transcription factor. Accordingly, 12% of residual nuclear GR was bound to chromatin in the absence of hormone treatment, as compared to 37% after induction with dexamethasone. These values are similar to previous estimates for the DNA-bound fraction of nuclear STAT1 and p53 (refs. 22,25). On a single-molecule basis, these percentages correspond to the fractions of time a GR is bound to DNA.

DNA residence times of transcription factors

Next we measured the *in vivo* residence time of individual GR dimer molecules bound to DNA in the presence of 100 nM dexamethasone, using the principle of detection by localization[29].

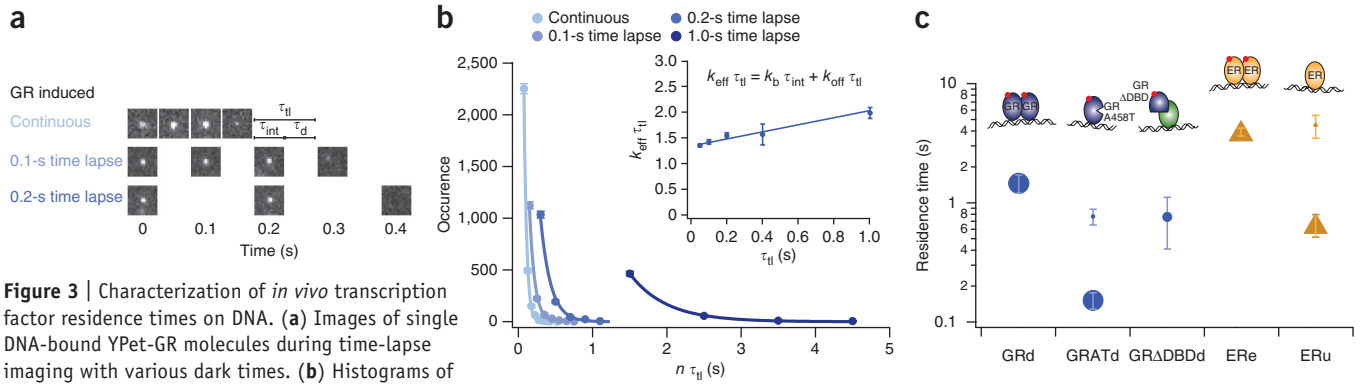

Figure 3 | Characterization of *in vivo* transcription factor residence times on DNA. (**a**) Images of single DNA-bound YPet-GR molecules during time-lapse imaging with various dark times. (**b**) Histograms of fluorescent 'on' times in different time-lapse conditions (n = 2,991 (0.05 s); n = 1,465 (0.1 s); n = 1,308 (0.2 s); n = 92 (0.4 s); n = 539 (1.0 s); data from 34 cells). Lines are fits by an exponential decay model with one effective rate constant (equation (3) in Online Methods). Inset, extracted effective rate constant as function of the time-lapse condition. Error bars, s.d. k_{eff}, effective rate constant; k_b, photobleaching rate constant; k_{off}, off-rate constant; τ_{tl}, duration of time-lapse; τ_{int}, camera integration time; τ_d, dark time. (**c**) Residence times of dimeric GR (GRd), the point mutant GR A458T incapable of dimerization (GRATd) and a mutant lacking the DNA binding domain (GRΔDBDd), all induced with 100 nM dexamethasone, and estrogen receptor (ER) induced with 100 nM β-estradiol (ERe) or uninduced ER (ERu) in MCF-7 cells. Symbol size is proportional to the fraction of molecules exhibiting a certain residence time or, for GR ΔDBD, the number of binding events relative to GRd. The cartoons illustrate the most abundant binding mode. Error bars, s.d. (Online Methods).

As mEos2 exhibits prolonged fluorescent dark states that might interfere with residence time measurements, here we used the bright yellow fluorescent protein YPet as a tag for GR in a plasmid allowing low expression in MCF-7 cells (Online Methods). We considered a molecule to be bound to DNA only if it stayed immobile for at least two consecutive frames (**Supplementary Video 7** and Online Methods)[29].

Owing to the fast photobleaching of fluorescent proteins, it is not possible to determine the residence time on the basis of continuous single-molecule tracking because both photobleaching and dissociation contribute to the loss of the fluorescent signal. Instead, we performed time-lapse illumination with a fixed camera integration time, τ_{int}, of 50 ms interspersed with dark periods, τ_d, of varying duration (**Fig. 3a**). This enabled us to extract the dissociation rate constant, k_{off}, and photobleaching rate constant, k_b, from the effective off-rate constant, k_{eff}, obtained from distributions of the measured fluorescence 'on' times of bound YPet-GR (**Fig. 3b** and Online Methods). We obtained $k_{off} = 0.69 \pm 0.11\ s^{-1}$ and $k_b = 26.8 \pm 0.5\ s^{-1}$ for dimeric GR. The GR residence time of 1.45 s (calculated as k_{off}^{-1}; **Supplementary Table 1**) falls in the same range as the fluorescence recovery time of 5 s initially measured in fluorescence recovery after photobleaching (FRAP) experiments[2,30] and is similar to the residence times of dye-labeled STAT1 and p53 recently obtained in single-molecule experiments[22,25]. The k_b of YPet is consistent with the value we found in a control experiment performed *in vitro* under comparable illumination conditions (**Supplementary Fig. 5**).

We then probed DNA binding of the monomeric GR by using a point mutant capable of nuclear import upon induction but incapable of dimerization (GR A458T)[31]. Notably, a simple model with one dissociation rate constant was not sufficient to fit the fluorescence 'on' time distributions of GR A458T (**Supplementary Fig. 6**). We therefore used a model describing a transcription factor that has two populations with different dissociation rate constants $k_{off,1}$ and $k_{off,2}$ and amplitudes A_1 and A_2 (equation (4) in Online Methods). We found that 97% ± 2% of GR A458T had a residence time of 0.15 s ± 0.02 s, tenfold faster than that of dimeric GR, and a second fraction of 3% ± 2% with a residence time of 0.76 s ± 0.12 s (± s.d.; **Fig. 3c** and **Supplementary Fig. 7**). To assign these components, we imaged a GR mutant lacking the DNA binding domain (GR ΔDBD), which had a single residence time of 0.76 s ± 0.35 s, comparable to the slow fraction of GR A458T (**Supplementary Figs. 7** and **8**). We therefore concluded that the 3% component of monomeric GR A458T molecules represents protein-protein interactions, not direct binding to DNA.

Next we measured the residence time of the closely related ER fused to YPet. Similarly to GR, ER can be induced by hormone treatment to dimerize and bind to cognate DNA sequences. In contrast to GR, ER is constitutively localized to the nucleus in MCF-7 cells[32]. Similarly to GR, we resolved a large fraction (87% ± 5%) of uninduced ER dissociating at a rate constant sixfold faster than that of the dimeric ER (**Fig. 3c** and **Supplementary Fig. 9**). Taken together, these results suggest that our method allows us to discriminate between three different modes of DNA binding, that is, dimeric, monomeric and indirect DNA binding through association with other transcription factors.

Spatiotemporal colocalization of two molecular species

We next analyzed spatiotemporal colocalization of GR and GRIP1 on DNA. GRIP1 is a coactivator for GR and other steroid receptors[33]. We performed the experiments in U2-OS cells that are commonly used for GR and GRIP1 studies because they do not express these factors endogenously[34]. This allows the exclusive expression of fluorescently labeled GR and GRIP1. YPet fusions of both proteins showed residence times comparable to that of GR measured in MCF-7 cells (**Supplementary Table 1** and **Supplementary Fig. 10**). For simultaneous observation of GR and GRIP1, we performed two-color single-molecule imaging by labeling GRIP1 with EGFP and GR with TagRFP-T. We alternated 488-nm and 560-nm laser excitation with 50 ms of integration time in the same light-sheet illumination plane (**Supplementary Video 8**). **Figure 4a** shows an example of spatiotemporal colocalization of GR and GRIP1 on DNA. By comparing the numbers of localizations per pixel and per second of GR and GRIP1 alone with the number of detected colocalization events,

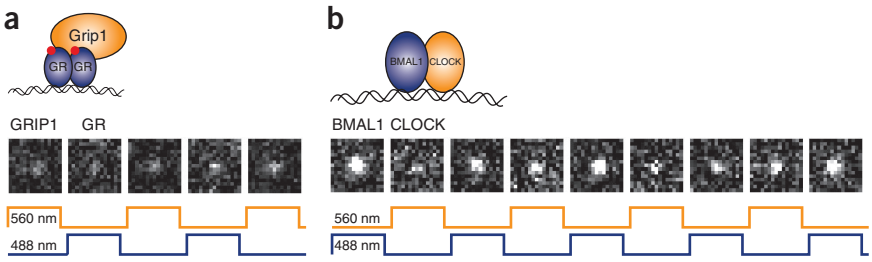

Figure 4 | Two-color imaging of two different molecular species at the single-molecule level. (**a**) Example of GR-GRIP1 colocalization. TagRFP-T–GR (blue trace) and EGFP-GRIP1 (orange trace) were alternately excited with 50-ms exposure time. (**b**) Example of BMAL1-CLOCK colocalization. TagRFP-T–BMAL1 (blue trace) and EGFP-CLOCK (orange trace) were alternately excited with 50-ms exposure time.

we estimated that colocalization events were ~80 times more likely than expected by chance.

Next we used the same fluorescent proteins to label BMAL1 and CLOCK, a transcription factor pair known to bind DNA as a heterodimer[35]. Both proteins showed colocalization events, consistent with the formation of a complex composed of BMAL1, CLOCK and largely stationary DNA (**Fig. 4b** and **Supplementary Video 9**). As observed for GR and GRIP1, colocalization events were two orders of magnitude more likely then expected by chance. Thus, RLSM can be used to probe the spatiotemporal colocalization of two different molecular species labeled with a fluorescent protein at the single-molecule level.

DISCUSSION

The vertical orientation of the illumination and detection objectives in our microscope introduces several advantages over the orthogonal geometry of objectives normally used in selective-plane-illumination instruments[19]. First, any commercial inverted microscope may be switched to a light-sheet illumination setup by adjusting the laser illumination beam path, replacing the condenser with a water-dipping objective and connected mirror and exchanging the sample stage with a piezo stage. Second, both objectives can be chosen with high NA. This allows for a very thin excitation light sheet (>0.5 µm) as well as a high efficiency of fluorescent light collection with the detection objective. Third, the reflecting mirror allows positioning of the horizontal light sheet close to the cover glass surface, leaving only a small gap of ~2 µm that cannot be illuminated. This gap is small enough to enable sectioning of most of the nucleus of mammalian cells, resulting in a high SBR of fluorescence imaging superior to those of wide-field and HILO illumination. Finally, there is no need for special observation chambers, as commercially available glass-bottom culture dishes can be used for both cell culture and imaging, simplifying experimental procedures[14,15].

The time-lapse approach we used to characterize transcription factor binding to DNA allows reliable measurements of residence times ranging from 50 ms (as given by the integration time) to several seconds. As this strategy does not rely on the detection of long continuous traces of a fluorescent molecule, it is well suited for the use of fast-photobleaching fluorescent protein labels. In fact, our time-lapse approach should prove advantageous compared to the analysis of continuous traces even when more photostable organic dyes are used as labels if the DNA-binding protein exhibits a residence time on the order of seconds. For longer time scales, both approaches have limitations because cellular movements prevent the reliable assignment of a continuously bound molecule in time-lapse illumination, and continuously fluorescing dyes become sparse as a result of photobleaching.

The increase in residence time of dimeric GR and ER over that of the monomeric transcription factor probably reflects stabilization of DNA binding by an associated partner. However, our observations are also compatible with a proportion of molecules remaining in the monomeric form, as the dynamics of a fast-dissociating fraction of molecules cannot be resolved if the majority of molecules dissociates slowly (**Supplementary Fig. 6**). In contrast, a small fraction of longer-bound molecules was resolved for monomeric GR and ER, which we could assign to an indirect binding mode to other protein factors for GR.

A common technique to study transcription factor dynamics is FRAP, which monitors the recovery of fluorescence in a bleached area. This area is replenished through diffusion and rebinding of unbleached fluorescent fusion proteins, which replace dissociated bleached molecules. With FRAP, an upper bound for the residence time of GR of 170 ms has been reported[36]; this is ninefold faster than what we measured for dimeric GR. However, the indirect assessment of residence times via reaction-diffusion models is error-prone, as experimental conditions including the geometry of the bleached volume, the fraction of free-diffusing molecules and photophysical properties of the fluorophore must be accurately determined[22,36–40]. The direct determination of transcription factor residence times by single-molecule approaches is not subject to these limitations. In addition, the single-molecule trajectories accessible with our method allow nanometer spatial accuracy and millisecond temporal accuracy of a molecular species. The types of real-time single-molecule experiments that our technique allows will facilitate detailed mechanistic studies of transcription initiation and provide the opportunity to probe the dynamic properties of molecular interactions *in vivo*.

METHODS

Methods and any associated references are available in the online version of the paper.

Note: Supplementary information is available in the online version of the paper.

ACKNOWLEDGMENTS

We acknowledge W. Min for his contribution in the early stage of this work. The pLV-tetO-Oct4 plasmid was provided by K. Hochedlinger (Howard Hughes Medical Institute and Harvard Stem Cell Institute), and MD2G and PAX2 plasmids were provided by D. Trono (Ecole Polytechnique Fédérale de Lausanne). We acknowledge funding from the US National Institutes of Health (X.S.X. (5R01EB010244-3 and 5R01GM096450-02) and T.M. (R01NS043915 and DP1OD003930-03)), Human Frontier Science Program (J.C.M.G.), fellowship for advanced researchers from the Swiss National Science Foundation (D.M.S.), Jane Coffin Childs postdoctoral fellowship (R.R.), National Science Scholarship from the Agency of Science, Technology and Research (A*STAR) of Singapore (Z.W.Z.) and Molecular Biophysics Training Grant Agency, US National Institutes of Health–National Institute of General Medical Sciences T32 GM008313 (A.R.C.). This work was performed in part at the Harvard Center for Nanoscale Systems, a member of the National Nanotechnology Infrastructure Network, which is supported by the US National Science Foundation under award ECS-0335765.

AUTHOR CONTRIBUTIONS

J.C.M.G. conceived and set up the reflected light-sheet microscope. J.C.M.G. and D.M.S. designed experiments. J.C.M.G. performed measurements and analyzed data. D.M.S. cloned fusion proteins, established cell lines and contributed to measurements and data analysis. J.C.M.G. and R.R. cloned mEos2-GR and mEos2-H4. R.R., Z.W.Z. and A.R.C. contributed to system setup. R.R. and Z.W.Z. contributed to light sheet characterization. R.R. and A.R.C. contributed to the analysis code. S.B. contributed to cloning. R.R., Z.W.Z. and S.B. contributed cells for initial performance tests. X.S.X. initiated the project. X.S.X. and T.M. supervised the project. J.C.M.G., D.M.S., T.M. and X.S.X. wrote the manuscript with contributions from all authors.

COMPETING FINANCIAL INTERESTS

The authors declare no competing financial interests.

1. Li, G.W. & Xie, X.S. Central dogma at the single-molecule level in living cells. *Nature* **475**, 308–315 (2011).
2. McNally, J.G., Müller, W.G., Walker, D., Wolford, R. & Hager, G.L. The glucocorticoid receptor: rapid exchange with regulatory sites in living cells. *Science* **287**, 1262–1265 (2000).
3. Fuda, N.J., Ardehali, M.B. & Lis, J.T. Defining mechanisms that regulate RNA polymerase II transcription *in vivo*. *Nature* **461**, 186–192 (2009).
4. Xie, X.S., Choi, P.J., Li, G.W., Lee, N.K. & Lia, G. Single-molecule approach to molecular biology in living bacterial cells. *Annu. Rev. Biophys.* **37**, 417–444 (2008).
5. Hammar, P. *et al.* The *lac* repressor displays facilitated diffusion in living cells. *Science* **336**, 1595–1598 (2012).
6. Goulian, M. & Simon, S.M. Tracking single proteins within cells. *Biophys. J.* **79**, 2188–2198 (2000).
7. Seisenberger, G. *et al.* Real-time single-molecule imaging of the infection pathway of an adeno-associated virus. *Science* **294**, 1929–1932 (2001).
8. Sako, Y., Minoghchi, S. & Yanagida, T. Single-molecule imaging of EGFR signalling on the surface of living cells. *Nat. Cell Biol.* **2**, 168–172 (2000).
9. Tokunaga, M., Imamoto, N. & Sakata-Sogawa, K. Highly inclined thin illumination enables clear single-molecule imaging in cells. *Nat. Methods* **5**, 159–161 (2008).
10. Huisken, J., Swoger, J., Del Bene, F., Wittbrodt, J. & Stelzer, E.H. Optical sectioning deep inside live embryos by selective plane illumination microscopy. *Science* **305**, 1007–1009 (2004).
11. Friedrich, M. *et al.* Detection of single quantum dots in model organisms with sheet illumination microscopy. *Biochem. Biophys. Res. Commun.* **390**, 722–727 (2009).
12. Ritter, J.G., Veith, R., Veenendaal, A., Siebrasse, J.P. & Kubitscheck, U. Light sheet microscopy for single molecule tracking in living tissue. *PLoS ONE* **5**, e11639 (2010).
13. Cella Zanacchi, F. *et al.* Live-cell 3D super-resolution imaging in thick biological samples. *Nat. Methods* **8**, 1047–1049 (2011).
14. Capoulade, J., Wachsmuth, M., Hufnagel, L. & Knop, M. Quantitative fluorescence imaging of protein diffusion and interaction in living cells. *Nat. Biotechnol.* **29**, 835–839 (2011).
15. Wu, Y. *et al.* Inverted selective plane illumination microscopy (iSPIM) enables coupled cell identity lineaging and neurodevelopmental imaging in *Caenorhabditis elegans*. *Proc. Natl. Acad. Sci. USA* **108**, 17708–17713 (2011).
16. Planchon, T.A. *et al.* Rapid three-dimensional isotropic imaging of living cells using Bessel beam plane illumination. *Nat. Methods* **8**, 417–423 (2011).
17. Tsai, S.Y. *et al.* Molecular interactions of steroid hormone receptor with its enhancer element: evidence for receptor dimer formation. *Cell* **55**, 361–369 (1988).
18. Aagaard, M.M., Siersbæk, R. & Mandrup, S. Molecular basis for gene-specific transactivation by nuclear receptors. *Biochim. Biophys. Acta* **1812**, 824–835 (2011).
19. Huisken, J. & Stainier, D.Y. Selective plane illumination microscopy techniques in developmental biology. *Development* **136**, 1963–1975 (2009).
20. Keppler, A. *et al.* A general method for the covalent labeling of fusion proteins with small molecules *in vivo*. *Nat. Biotechnol.* **21**, 86–89 (2003).
21. Los, G.V. *et al.* HaloTag: a novel protein labeling technology for cell imaging and protein analysis. *ACS Chem. Biol.* **3**, 373–382 (2008).
22. Mazza, D., Abernathy, A., Golob, N., Morisaki, T. & McNally, J.G. A benchmark for chromatin binding measurements in live cells. *Nucleic Acids Res.* **40**, e119 (2012).
23. Manley, S. *et al.* High-density mapping of single-molecule trajectories with photoactivated localization microscopy. *Nat. Methods* **5**, 155–157 (2008).
24. English, B.P. *et al.* Single-molecule investigations of the stringent response machinery in living bacterial cells. *Proc. Natl. Acad. Sci. USA* **108**, E365–E373 (2011).
25. Speil, J. *et al.* Activated STAT1 transcription factors conduct distinct saltatory movements in the cell nucleus. *Biophys. J.* **101**, 2592–2600 (2011).
26. Akhtar, A. & Gasser, S.M. The nuclear envelope and transcriptional control. *Nat. Rev. Genet.* **8**, 507–517 (2007).
27. Thompson, R.E., Larson, D.R. & Webb, W.W. Precise nanometer localization analysis for individual fluorescent probes. *Biophys. J.* **82**, 2775–2783 (2002).
28. Bancaud, A. *et al.* Molecular crowding affects diffusion and binding of nuclear proteins in heterochromatin and reveals the fractal organization of chromatin. *EMBO J.* **28**, 3785–3798 (2009).
29. Elf, J., Li, G.W. & Xie, X.S. Probing transcription factor dynamics at the single-molecule level in a living cell. *Science* **316**, 1191–1194 (2007).
30. Becker, M. *et al.* Dynamic behavior of transcription factors on a natural promoter in living cells. *EMBO Rep.* **3**, 1188–1194 (2002).
31. Heck, S. *et al.* IκBα-independent downregulation of NF-κB activity by glucocorticoid receptor. *EMBO J.* **16**, 4698–4707 (1997).
32. Zava, D.T., Chamness, G.C., Horwitz, K.B. & McGuire, W.L. Human breast cancer: biologically active estrogen receptor in the absence of estrogen? *Science* **196**, 663–664 (1977).
33. Hong, H., Kohli, K., Trivedi, A., Johnson, D.L. & Stallcup, M.R. GRIP1, a novel mouse protein that serves as a transcriptional coactivator in yeast for the hormone binding domains of steroid receptors. *Proc. Natl. Acad. Sci. USA* **93**, 4948–4952 (1996).
34. Beck, M. *et al.* The quantitative proteome of a human cell line. *Mol. Syst. Biol.* **7**, 549 (2011).
35. Gekakis, N. *et al.* Role of the CLOCK protein in the mammalian circadian mechanism. *Science* **280**, 1564–1569 (1998).
36. Sprague, B.L. *et al.* Analysis of binding at a single spatially localized cluster of binding sites by fluorescence recovery after photobleaching. *Biophys. J.* **91**, 1169–1191 (2006).
37. Beaudouin, J., Mora-Bermúdez, F., Klee, T., Daigle, N. & Ellenberg, J. Dissecting the contribution of diffusion and interactions to the mobility of nuclear proteins. *Biophys. J.* **90**, 1878–1894 (2006).
38. Mueller, F., Mazza, D., Stasevich, T.J. & McNally, J.G. FRAP and kinetic modeling in the analysis of nuclear protein dynamics: what do we really know? *Curr. Opin. Cell Biol.* **22**, 403–411 (2010).
39. Stavreva, D.A., Varticovski, L. & Hager, G.L. Complex dynamics of transcription regulation. *Biochim. Biophys. Acta* **1819**, 657–666 (2012).
40. Mueller, F., Morisaki, T., Mazza, D. & McNally, J.G. Minimizing the impact of photoswitching of fluorescent proteins on FRAP analysis. *Biophys. J.* **102**, 1656–1665 (2012).

ONLINE METHODS

Optical setup for RLSM. The reflected light-sheet microscope was integrated into an inverted microscope (IX71, Olympus) (**Supplementary Fig. 1a**). Illumination lasers (405 nm, 50 mW, Electra-40, Laserglow; 488/514 nm, 1,000 mW, Innova300, Coherent; 560 nm, 1,000 mW, VFL-P-1000-560, MPB Communications; actual intensity was set to 3 mW in the sample plane) were collimated and colinearly combined via dichroic beam splitters. Shutters (LS3M2, Uniblitz) were used to control the active laser times. A telescope of two cylindrical lenses (f = 40 mm, LJ1402L1-A and f = 400 mm, LJ1363L1-A, both Thorlabs) created an expanded and collimated line that overfilled the back aperture of the vertical illumination objective (LUMPLFLN 40× water, 0.8 NA, Olympus) and was focused to a diffraction-limited light sheet. A third cylindrical lens (f = 150 mm, LJ1629L1-A, Thorlabs) was used to control the lateral extension of the light sheet. A spherical iris in front of the illumination objective allowed reduction of the illumination line dimensions and thus the FWHM of the light sheet. A tipless AFM cantilever (HYDRA2R-100N-TL-10, Nanoscience) was mounted to the illumination objective via a custom-designed holder (**Supplementary Fig. 1b**,**c**). The disposable AFM cantilever was custom-coated with a 1 nm Ti layer followed by 40 nm Al layer by thermal evaporation. A manual x-y stage (ST1XY-S, Thorlabs) and a z stage (423, Newport) allowed simultaneous positioning of illumination objective and cantilever holder with respect to the detection objective (UPlanApo 100×/1.35 oil or UPlanSApo 100×/1.4 oil, both Olympus). Fluorescent light (filters sets for mEos2: dichroic Di01-R561, filters Brightline 617/73 and Edgebasic long-wave-pass 561, Semrock; YPet: dichroic FF495-Di03, Semrock and filter HQ545/30, Chroma; EGFP/TagRFP-T: dichroic Di01-R488/561 and filter FF01-523/610, Semrock) was focused onto a back-illuminated electron-multiplying charge-coupled device (EMCCD) camera (iXon+, DU-897E-CSO-BV, Andor). Bright-field illumination was achieved using the microscope source, which was coupled into the illumination objective using a dichroic (FF593-Di03, Semrock). The sample dish (Delta-T, Bioptechs) was mounted onto a custom-designed manual x-y stage, in which a thermal control unit (Delta-T, Bioptechs) was integrated to control the sample temperature (36 °C). An objective heater (FAB6318x, 1000 Oaks Optical) aided in thermal control. An x-y-z piezo stage (Nano-Bio3200, Mad City Labs), controlled by LabVIEW software, was used for precision positioning and vertical scanning of the sample. The microscope, shutters and EMCCD camera were controlled by MetaMorph software.

Design of the cantilever holder. The cantilever holder consisted of four stainless steel cylinders. The first unit was stably mounted to the objective, and the other units were successively connected via two miniature linear guides per plane (MR3MNSS1V0N15L-2.5-2.5, Precision Alliance), enabling movement of the fourth cylinder in three dimensions with respect to the objective. A micrometer drive (DM11-5, Newport) counteracted by a small spring was used for precise position control of each plane. The fourth cylinder held a lug with a small groove that accommodated the AFM cantilever. High-vacuum grease (Dow Corning) was used to reversibly fix the cantilever and ensured stable mounting after ~10 min settling time.

DNA constructs. The Halo tag sequence was purchased from Promega (pHTN HaloTag CMV-neo Vector), and SNAP tag sequence was purchased from New England Biolabs (pSNAPf-Vector). The mEos2-GR and mEos2-H4 constructs were generated by fusing GR sequence to that of mEos2 (ref. 41) in the pSNAPf vector (New England Biolabs). YPet[42], EGFP and Tag-RFP-T[43] fusion constructs were generated by using pLV-tetO-Oct4 as a backbone (provided by K. Hochedlinger). Briefly, the Oct4 coding sequence was replaced with coding sequences of the different fusion proteins. All fusion constructs were generated as N-terminal fusions of the fluorescent protein to each protein of interest. Sequence encoding the YPet-GR A458T variant was generated by site-directed mutagenesis. To generate DNA-binding domain deletion mutants of GR, we generated and ligated PCR products of sequences upstream and downstream of the DNA binding domain (as defined in the UniProt database, http://www.uniprot.org/). The primers used to make the different constructs can be found in **Supplementary Table 2**.

Generation of stable cell lines. MCF-7 cells stably expressing mEos2, mEos2-GR and mEos2-H4 were generated by transfection of plasmids with Polyplus reagent and selected with puromycin for 2–3 weeks. All other cell lines were generated by lentiviral transduction. Briefly, each construct was cotransfected with the packaging plasmids MD2G and PAX2 (provided by D. Trono) in 293T cells using Lipofectamine 2000. Supernatants were collected 48 h after transfection and filtered through 0.45-µm low protein-binding filters (Pall corporation). Supernatant (1–2 ml) was used to transduce 3×10^4–5×10^4 U2-OS or MCF-7 cells, and the medium was changed 1–3 d after transduction.

Cell culture. U2-OS cells were cultured in high-glucose DMEM (Gibco) supplemented with 10% FBS (FBS), 1% penicillin/streptomycin and 2 mM GlutaMAX (Gibco). MCF-7 cells were cultured in a-MEM (Gibco) supplemented with 10% FBS, 1% penicillin/streptomycin, 2 mM L-glutamine (Gibco), 1 mM sodium pyruvate and 100 mM non-essential amino acids (mMCF7). To achieve uninduced conditions for GR or ER, we grew cells for at least 1 d in mMCF7 with charcoal-stripped FBS (mMCF7–) and 1 d in mMCF7– without phenol red. Just before imaging, OptiMEM was used to wash the cells once and maintain them for imaging. To induce the activity of GR and ER, we treated cells for 30 min with 100 nM dexamethasone or 100 nM β-estradiol, respectively. For the U2-OS cell lines stably expressing BMAL1 and CLOCK fusion constructs, cells were first synchronized by serum shock. Briefly, cells were first incubated in suspension in a 1:1 mix of complete culture medium and FBS for 1 h before the medium was changed to complete cell culture medium (phenol red–free DMEM supplemented with 10% FBS, 1% penicillin-streptomycin and 2 mM L-glutamine (Gibco)). Cells were then incubated for 24 h before imaging and were imaged without washing or change of buffer, except for the two-color experiments, in which OptiMEM was used for imaging.

Determination of the laser beam profile. Before reflection, the laser beam profile was characterized by imaging the intensity cross-section at various distances from the focus onto the EMCCD camera and determining the FWHM from Gaussian fits to each intensity distribution. For characterization of the beam

profile after reflection, fluorescent beads (TetraSpeck microspheres, 100-nm diameter, Invitrogen) attached to fixed HeLa cells for elevation above the sample surface were scanned across the beam at various distances from the focus, controlled via the piezo *x*-*y*-*z* stage. Fluorescence emitted by the beads was projected onto the EMCCD camera, and beads were kept in focus by moving the detection objective with a piezo *z* stage (PIFOC, Physik Instrumente). The FWHM of the laser beam was determined from Gaussian fits to the resulting intensity distributions. Errors of the FWHM are the s.d. of the parameter obtained from the fits.

Data acquisition. Cells were imaged in Delta-T glass-bottom dishes (Bioptechs). Dishes were washed once with OptiMEM and imaged in OptiMEM at 36 °C for up to 45 min (GR and GR variants), 60 min (uninduced ER) or 120 min (induced ER).

Data acquisition with RLSM is straightforward and comparable to that for other single-molecule assays. Exchange of the AFM cantilever and positioning with respect to the light-sheet focus can be achieved within 20 min. Once in place, a cantilever typically can be used for 5 d of imaging, with only minor position adjustments for each sample. Positioning of the cantilever next to a cell is precisely controlled by the *x*-*y*-*z* piezo stage and achieved within 1 min without perforating the cell membrane.

The power of all illumination lasers was kept below 3 mW, which corresponds to ~5 kW/cm^2 in the focal plane of the illumination objective. This is comparable to the laser power density used in other live-cell single-molecule microscopy assays[44].

Single-molecule tracking. Single-molecule tracking was achieved essentially as described[29]. In brief, images were background subtracted with Matlab (2010b, MathWorks). After additional smoothing, the coarse position of fluorescent molecules was determined from pixel values exceeding a threshold of 4 × s.d. over the background. The fine position of particles was obtained by two-dimensional Gaussian fitting on the initial background-subtracted image.

Comparison of RLSM and HILO microscopy. Cells were imaged in OptiMEM at room temperature. The position, peak intensity and background level of single molecules were determined by two-dimensional Gaussian fitting on the original uncorrected image. The SBR was defined as signal divided by the background level above the camera dark offset[45]. For both RLSM and HILO microscopy, the SBRs of all molecules in a nuclear *z* section of a cell were combined into a histogram, whose median value was used to calculate the ratio between RLSM and HILO microscopy SBR for this *z* section.

Extraction of diffusion components. To accurately determine the diffusion properties of labeled molecules from short tracks, arising from photobleaching or diffusion out of the focal plane, we analyzed cumulative distribution functions of squared displacements instead of the mean squared displacement[46]. The probability density $f(x^2 + y^2)$ of squared displacements $(x^2 + y^2)$ for Brownian diffusion is given by

$$f(x^2+y^2)=\frac{1}{4\pi D\tau}\exp\left(-\frac{(x^2+y^2)}{4D\tau}\right)$$

where D denotes the diffusion constant and τ the camera integration time. Integration of the probability density yields the cumulative distribution function $F(x^2 + y^2)$

$$F(x^2+y^2)=\int\frac{1}{4\pi D\tau}\exp\left(-\frac{(x^2+y^2)}{4D\tau}\right)\mathrm{d}(x^2+y^2)$$
$$=1-\exp\left(-\frac{(x^2+y^2)}{4D\tau}\right) \quad (1)$$

or

$$F(X)=A_1\left(1-\exp\left(-\frac{X}{D_1}\right)\right)+A_2\left(1-\exp\left(-\frac{X}{D_2}\right)\right)$$
$$+(1-A_1-A_2)\left(1-\exp\left(-\frac{X}{D_3}\right)\right) \quad (2)$$

in the case of three different diffusion components, where $X = (x^2 + y^2)/(4\tau)$ and A denotes amplitude.

To avoid bias toward slowly moving particles that remain visible for longer times, we counted only the first displacement of each track. To avoid false assignments of molecules to another track for fast molecules, we set an upper limit of 6 pixels for the maximum squared displacement of a molecule. This limit was accounted for by replacing the last term in equation (2) with

$$(1-A_1-A_2)\left(\exp\left(-\frac{X}{D_3}\right)-\exp\left(-\frac{C_1}{D_3}\right)\right)\Big/\left(\exp\left(-\frac{C_2}{D_3}\right)-\exp\left(-\frac{C_1}{D_3}\right)\right)$$

where the constants C_1 and C_2 are given by the lower and upper limits for the squared displacements of 0 and 6 pixels[47]. Fitting was performed in Igor Pro (v.6.2, WaveMetrics), with a nonlinear least-squares fitting procedure. Errors were calculated as the s.d. of parameters obtained from fits to 2,000 random subsets of the displacements, each comprising 80% of the original data.

Determination of off-rate constants. We considered molecules localized for at least two consecutive frames within 0.5 pixels (1 pixel in two-color experiments) as bound molecules. Localizations visible in only one frame were discarded to avoid counting slowly moving molecules. We allowed one dark frame within a trajectory to account for rare blinking events of the fluorescent protein at an illumination time of 50 ms.

During the monitoring of a fluorescent bound transcription factor, the fluorescent signal (fluorescent 'on' state) terminates because of two Poisson-distributed processes: photobleaching with rate constant k_1 and dissociation with rate constant $k_2 = k_{off}$. The photobleaching rate k_1 is proportional to the light intensity and thus dependent on the frame time τ_{int} and time-lapse time τ_{tl}: $k_1 = k_b\tau_{int}/\tau_{tl}$. Overall, the distribution of fluorescent 'on' times $f_1(t)$ follows an exponential function with the effective off-rate constant $k_{eff} = (k_1 + k_2) = (k_b\tau_{int}/\tau_{tl} + k_{off})$

$$f_1(t)=A\exp(-k_{\mathrm{eff}}t)=A\exp\left(-\left(k_b\frac{\tau_{\mathrm{int}}}{\tau_{\mathrm{tl}}}+k_{\mathrm{off}}\right)t\right) \quad (3)$$

To obtain the dissociation rate constant k_{off}, equation (3) was fitted to distributions of fluorescent 'on' times measured at

doi:10.1038/nmeth.2411

different time-lapse times, yielding k_{eff}. k_{eff} τ_{tl} was then plotted as function of the time-lapse time. In this plot, k_{off} is given by the slope and $k_b\tau_{int}$ by the y intersect.

Alternatively, we obtained the values for k_{off} and k_b by a global fit of equation (3) to all fluorescent 'on' time distributions at different time-lapse times, which yielded similar values.

If the linear extrapolation of k_{eff} deviates from a line, this suggests that two dissociation rate constants are resolved (**Supplementary Fig. 5**). In this case the distribution of fluorescent 'on' times was fit by the double-exponential function

$$f_2(t) = A\left(B\exp\left(-\left(k_b\frac{\tau_{int}}{\tau_{tl}} + k_{off,1} \right) t \right) + (1-B)\exp\left(-\left(k_b\frac{\tau_{int}}{\tau_{tl}} + k_{off,2} \right) t \right) \right) \quad (4)$$

with dissociation rate constants $k_{off,1}$ and $k_{off,2}$. Here, B denotes the fraction of molecules unbinding with off-rate $k_{off,1}$. Errors for dissociation rate constants and amplitudes are the s.d. of the parameters obtained from fits to equation (3) or equation (4).

41. McKinney, S.A., Murphy, C.S., Hazelwood, K.L., Davidson, M.W. & Looger, L.L. A bright and photostable photoconvertible fluorescent protein. *Nat. Methods* **6**, 131–133 (2009).
42. Nguyen, A.W. & Daugherty, P.S. Evolutionary optimization of fluorescent proteins for intracellular FRET. *Nat. Biotechnol.* **23**, 355–360 (2005).
43. Shaner, N.C. *et al.* Improving the photostability of bright monomeric orange and red fluorescent proteins. *Nat. Methods* **5**, 545–551 (2008).
44. Jones, S.A., Shim, S.H., He, J. & Zhuang, X. Fast, three-dimensional super-resolution imaging of live cells. *Nat. Methods* **8**, 499–508 (2011).
45. Moerner, W.E. & Fromm, D.P. Methods of single-molecule fluorescence spectroscopy and microscopy. *Rev. Sci. Instrum.* **74**, 3597 (2003).
46. Schütz, G.J., Schindler, H. & Schmidt, T. Single-molecule microscopy on model membranes reveals anomalous diffusion. *Biophys. J.* **73**, 1073–1080 (1997).
47. Gebhardt, J.C.M., Clemen, A.E., Jaud, J. & Rief, M. Myosin-V is a mechanical ratchet. *Proc. Natl. Acad. Sci. USA* **103**, 8680–8685 (2006).